Transactions on Engineering and Computing Sciences - Vol. 13, No. 02
Publication Date: April 25, 2025
DOI:10.14738/tmlai.1302.18449.
Qattan, N. A., Kada, B., & Al-Bahi, A. M. (2025). Numerical Investigation of Sand Erosion Effects on the T-56 Compressor Blade with Changing Parameters. Transactions on Engineering and Computing Sciences, 13(02). 62-83.

Numerical Investigation of Sand Erosion Effects on the T-56 Compressor Blade with Changing Parameters

Nizar A. Qattan

Belkacem Kada

Ali M. Al-Bahi

ABSTRACT

In the Gulf Cooperation Council (GCC) region, Lockheed C-130 aircraft are frequently exposed to sand and particle erosion. This harsh and corrosive environment causes the deterioration of the rotor blades' leading and trailing edges, which results in airfoil deformation, engine performance degradation, and a shorter lifespan. The present paper aims to model, simulate, and analyze the effects of sand erosion on a Lockheed T-56 engine compressor operating in such harsh environments. The study provides valuable insights into the effects of sand erosion on turbomachinery. It emphasizes developing effective mitigation strategies to guarantee optimal engine performance and longevity in harsh environments. Numerical models are developed and applied to calculate the surface erosion in turbomachinery, which helps to predict particle trajectories in turbomachinery passages and calculate impact rates, velocities, and angles. Profile data is created from new and eroded blades of the T-56 first-stage compressor using a 3D scan. The analysis results reveal that particle concentration has the greatest effect on blade erosion rate, whereas particle size has a lesser influence on all other measured parameters.

Keywords: computational fluid dynamics, turbomachinery, transonic compressor, T-56 engine compressor, transport equations, Eulerian approach, Turbulence models, shear stress transport model, Finnie's Model.

INTRODUCTION

The high sand and dust erosion can negatively impact Turbomachinery's performance and lifespan in some regions. When these particles collide with a wall's surface, it might result in mechanical damage. This type of erosion is a multi-physics problem, including the interplay of the flow field, particle trajectory, and wall deformation, and it is commonly related to gas-solid two-phase turbulent flow. The intricate three-dimensional flow and rotor-stator interaction during takeoff and landing make jet engines especially vulnerable to particle ingestion, which can cause significant damage to the compressor of aircraft engines. Erosion from sand and dust is exacerbated by the conditions depicted in Fig. 1 [1], which include a rise in pressure, temperature, and air mass velocity. Recent interest in these phenomena has prompted more studies into how to maintain best and enhance the performance of industrial machinery.

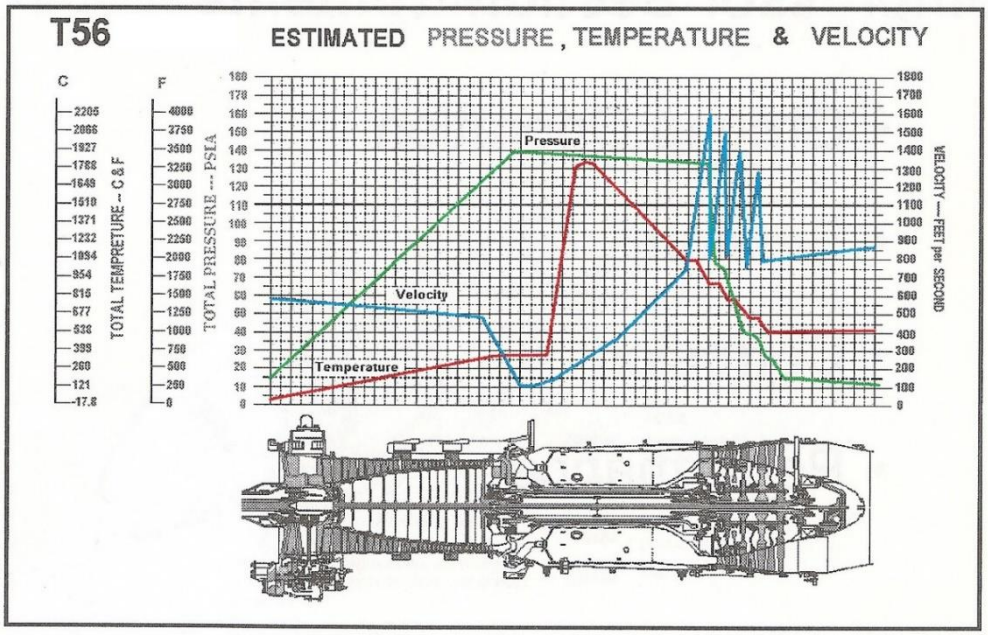

Fig 1: Schematic of Power Section Air Flow [1]

The erosive wear of compressor blades is a topic that has been the focus of numerous studies in scientific literature. Particle trajectories and flow field modifications in a single-stage axial flow compressor were numerically analyzed by Suzuki et al. [2]. They determined that the blade's leading edge and pressure surface experienced the most severe degradation because of the first collision. Subsequently, Suzuki and Yamamoto [3] created a 3D sand erosion prediction system and discovered that the blade's leading edge and pressure side are particularly vulnerable to erosion. Pressure surfaces and the impeller of the compressor experience the most erosion due to particle impacts, as determined by Tabakoff and Elfeki [4]. On the other hand, numerous studies have recently investigated the use of coating materials to stop erosion. Hardened steel (17-4 PH) was subjected to sand erosion tests by Koul et al. [5], who used a variety of techniques, including cryogenic treatment, ion implantation, vapor deposition, and Electron Beam Physical Vapor Deposition (EBPVD) to determine which coating material would be most effective. They found TiN coatings deposited by PVD were the most resistant to erosion, followed by EBPVD (16 μm) coatings that exhibited the greatest erosion resistance at 30° and 90° impingement angles, respectively. According to a comprehensive study by Muboyadzhyan [6] on Ion plasma coating prepared by hardened metal compounds, the best corrosion resistance was found for titanium alloys and compositions based on compressor steels, respectively. The effect of different stoichiometric compositions of (Ti, Cr) N Nano layer coatings placed on 17-4PH, Ti-6Al-4V, and Inconel 718, as well as Nano layer thickness on particle erosion was studied by Reedy et al. [7]. At a 90° angle of particle impingement, they discovered that uncoated samples performed better than coated ones. However, at a 30° angle of impingement, (Ti, Cr) N coatings with minimal microstructure bias performed better than TiN coatings. Simon and Litt use data from the T700-GE-701C engine and the Kalman filter as an estimator with data input from the engine's sensors. [8] devised a technique to estimate compressor efficiency decline. To monitor the wear and erosion of compressor blades in sandy

conditions, they created a tracking tool to monitor performance variance. Comparing simulated results with the mean line compressor performance model, Hameed et al. [9] examined performance loss in compressors due to blade attrition induced by ingested particles. Erosion causes blade surface roughness and tip clearance, which reduce adiabatic efficiency by 3–4%. Overall compressor performance and the influence of erosion on individual stages were reported by Lakshminarasimha et al. [10], who also established a model to assess the effects of erosion in multistage compressors. They determined that erosion had a greater impact on the compressor's initial stage than on later stages. W. Tabakof [11] found that most erosion in helicopter engines (when equipped with an inlet particle separator) occurs at the tip, close to the leading edge. He also found that erosion alters the pressure distribution across the blades and leads to tip leaks, negatively impacting engine efficiency.

The purpose of the present study is to develop a simulation tool for numerical analysis of the impact of erosion on the performance of a transonic compressor rotor such as T-56. To the authors' best knowledge, this is the first investigation into the effects of erosion on the performance of a T-56 transonic compressor rotor. The bow shock wave could affect the transonic rotor while it functions, changing the erosion pattern. The authors used a validation strategy derived from their earlier work on the NASA rotor 37 geometry [12] to verify the accuracy of the computational model used in this investigation. As no experimental data were available for the current geometry, the validation approach was essential to confirm the accuracy and reliability of the numerical results. Following the validation, the impact of erosion on the rotor's performance was studied by altering the particle size and number used. This allowed investigating the sensitivity of the rotor's performance to different levels of erosion, providing valuable insights into the impact of erosion on the transonic compressor rotor's performance.

SIMULATION AND GEOMETRICAL DETAILS

The purpose of this study is to analyze how erosion rate affects the compression ratio of the T-56 engine. To begin, a computational model of NASA's rotor 37 was created using data from prior studies [12]. Then, numerical simulations were checked against experimental data and a computer-based model was used to analyze the compressor rotor. Fig. 2 illustrates the geometrical model of the T-56 engine compressor used in this study.

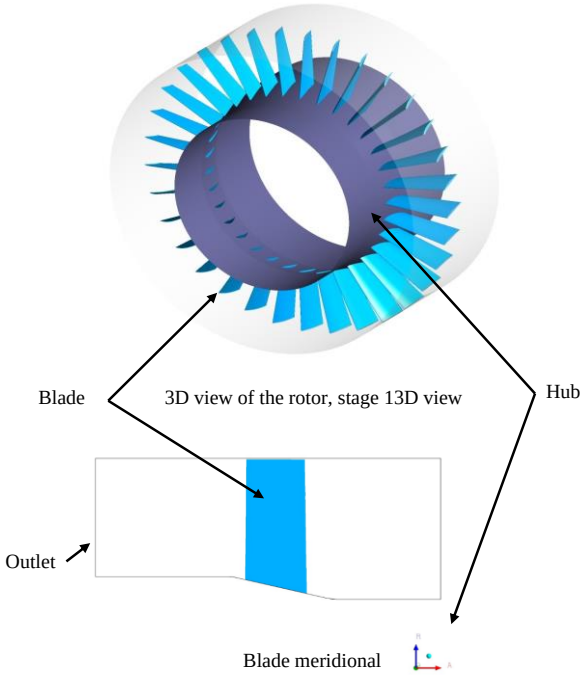

Fig 2: Geometry of the T-56 Engine First Compressor Rotor

Computational Model

Governing Equations:

A numerical study is conducted to estimate the erosion rate of the T-56 engine compressor using numerical analysis, considering several factors including the pressure ratio across the rotor P_r, solid particle mass concentration P_c, and particle size d_P. The Eulerian method is used to solve the two-phase solid-fluid (sand-air) transport equations in steady-state form. Equations (1) to (6) outline the Eulerian methodology utilized in this investigation [13].

Continuity Equation for Solid and Fluid Phase:

$$\boldsymbol{\nabla}.\left(C_f \rho_f \, \boldsymbol{V_f}\right) = 0 \tag{1}$$

$$\boldsymbol{\nabla}.\left(\boldsymbol{C_s \rho_s} \, \boldsymbol{V_s}\right) = \mathbf{0} \tag{2}$$

Continuity Equation for Solid and Fluid Phase:

$$\boldsymbol{\nabla}.\left(\boldsymbol{C_f \, \rho_f V_f \, V_f}\right) = -\boldsymbol{C_f \, \nabla P} + \boldsymbol{\nabla}.\left(\boldsymbol{C_f \tau_f}\right) + \boldsymbol{C_f \rho_f \, g} + \boldsymbol{R} + \boldsymbol{C_f \rho_f} \left(\boldsymbol{F_f} + \boldsymbol{F_{l,f}} + \boldsymbol{F_{vm_f}}\right) \tag{3}$$

$$\boldsymbol{\nabla}.\left(C_s \, \rho_s \mathbf{V_s} \, \mathbf{V_s}\right) = -C_s \, \nabla P + \boldsymbol{\nabla}.\left(C_s \boldsymbol{\tau_s}\right) + C_s \rho_s \, \mathbf{g} + \mathbf{R} + C_f \rho_f \left(\mathbf{F_f} + \mathbf{F_{l,s}} + \mathbf{F_{vm,s}}\right) \tag{4}$$

where $\boldsymbol{\tau_f}, \mathbf{V_f}, \boldsymbol{\tau_s}, \mathbf{V_s}$ denote the shear stress and velocity vector tensors for the fluid and solid phases, respectively. C_f, C_s are the fluid and solid volume concentrations, while ρ_f, ρ_s denote the densities of the fluid and solid phases.

The interaction force between the two phases is represented by $\boldsymbol{R}$ and the mean value of pressure for the interface solid-fluid phases is denotes by $\boldsymbol{P}$ [14]. In addition, $\mathbf{F_l}$ represents the lift force and $\mathbf{F_{vm,s}}$ is the virtual mass force per unit mass for both phases. The relation given by Eq. (5) is used to compute the lift force for solid phases $\mathbf{F_{l,s}}$, which is equal and opposite to the lift force for fluid phases $\mathbf{F_l}$, $\boldsymbol{s} = -\mathbf{F_{l,f}}$

$$\mathbf{F_l}, \boldsymbol{s} = -0.5\rho_f \alpha_s \left(\boldsymbol{V_f} - \boldsymbol{V_s}\right) \times (\nabla . \mathrm{V_f}) \tag{5}$$

The virtual mass effect causes the solid phase to accelerate through the fluid phase, giving rise to the virtual mass force $\mathbf{F_{vm,s}}$. This force is computed using Eq. (6).

$$\mathbf{F_{vm,s}} = 0.5\ \alpha_s \rho_f \left(\frac{d_f}{dt}\left(\ V_f\right) - \frac{d_s}{dt}\left(V_s\right)\right) \tag{6}$$

In the literature, one-way coupling and two-way coupling are the two most common techniques for solving the fluid-solid phase coupling problem [15]. The selection of the coupling technique is based on the value of β. When β is less than 0.14, one-way coupling is more suitable, while two-way coupling is preferred when β is greater than or equal to 0.14. The value of β can be calculated using Eq. (7).

$$\beta = \frac{C_s \rho_s}{C_f \rho_f} \tag{7}$$

This study's primary objective is to predict the erosion rate, which has a significant impact on the wall surface. The accurate estimation of wear rate density i.e., the prediction of the boundary layer, and the capture of recirculation regions near the wall are crucial to the study and present significant challenges. Flow features near walls, including boundary layers, cannot be precisely resolved by turbulence models, which rely on wall functions instead. Several studies [16-17-18] have utilized the shear stress transport model (SST model) to predict the near-wall phenomenon for rotating devices to address this issue. As a result, the $SST\ k-\omega$ turbulence model has been used to model turbulence in this investigation. Additional information on the modeling can be found elsewhere [19].

Erosion Model:

The impact of particulates on the walls results in surface deterioration, which erodes the casing material. This erosion is affected by a variety of particle parameters such as the turbulent field, multiphase effects (including dampening due to liquid film and erosion shield due to solid accumulation), the effect of local flow cavities caused by material elimination, and the wall material's properties. Hutchings [20] suggested that particle impact angle and velocity are significant eroding factors and proposed the following relationship

$$E = \ kV_p^n\ f(\gamma) \tag{8}$$

where E is a dimensionless mass, V_p denotes the particle velocity, and $f(\gamma)$ is the impact angle in radians. The value of n ranges from 2.3 to 2.5 based on the nature of the metal of the casing.

Since the experimental results needed to tune up the model parameters vary depending on the conditions, it is impossible to construct a universal model for erosion. To anticipate wear, the current study uses a model proposed by Finnie [21] based on his investigation of ductile materials for the value of n= 2. This model is related to the kinetic energy of particles.

$$E = kV_p^2 f(\gamma) \tag{9}$$

with

$$f(\gamma) = \frac{1}{3}\cos^2\gamma \ \ if \tan\gamma > \frac{1}{3}$$
$$f(\gamma) = \sin 2\gamma - 3\sin^2\gamma \ \ if \tan\gamma \leq \frac{1}{3} \tag{10}$$

Computational Mesh:

The ANSYS Turbo-Grid console is used for discretizing the rotating domain with hexahedral mesh elements. Fig. 3 displays the mesh of the rotor geometry where the interface boundaries have one ratio to one node connection to reduce interpolation losses. To ensure consistency at the interface, the same meshing topology is utilized for both the rotating and stationary domains [22]. The topology employed for the computational domains is based on O-grids [22]-[17]. Fig 3 represents the mesh topology and the distribution of the nodes.

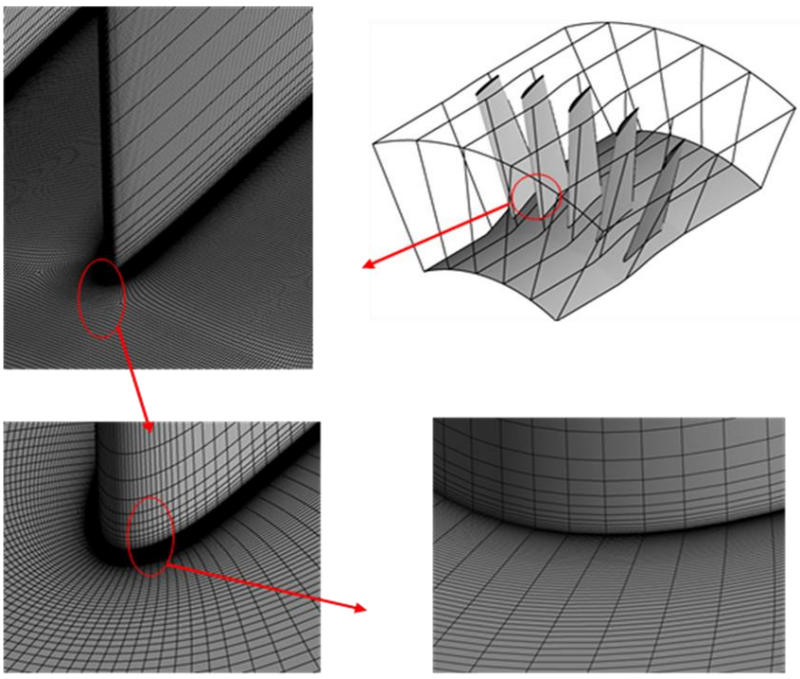

Fig 3: Mesh Distribution on the Hub and Blade

To ensure an accurate near-wall mesh and control the y^+ value, several O-grid topologies were employed. To fully utilize the capabilities of the SST turbulence model, a y^+ coefficient less than 1 was maintained for all simulations in both stationary and rotating domains [19]. The value of y+ depends on the flow length scale L, Reynolds number, and Δy, which is the distance of the

first node from the wall. To estimate the value of y^+ and obtain an optimal value, Eq. (11) is used [22-23].

To ensure an accurate near-wall mesh and control the y^+ value, several O-grid topologies were employed. To fully utilize the capabilities of the SST turbulence model, a y^+ coefficient less than 1 was maintained for all simulations in both stationary and rotating domains [19]. The value of y+ depends on the flow length scale L, Reynolds number, and Δy, which is the distance of the first node from the wall. To estimate the value of y^+ and obtain an optimal value, Eq. (11) is used [22-23].

$$\Delta y = L\, y^+ \sqrt{74}\, Re_L^{-\frac{13}{14}} \tag{11}$$

However, because this equation was developed for flow over flat plates, its ability to predict initial Δy estimates for geometries other than flat plates is limited. Consequently, the optimal value of y^+ can be determined for a given set of boundary conditions by modifying the values of Δy through a series of iterations. Acquiring a definite value of y^+ is not enough for a turbulence model to work accurately. A certain value for the minimum number of nodes (n_{min}) is also required within the boundary layer thickness (δ). For the SST turbulence model, the condition for (n_{min}) is given in Eq. (12) [22].

$$\begin{cases} y_n(n_{mi}) \le \delta \\ for\ SST\ n_{min} = 15 \\ y_n(15) \le \delta \end{cases} \tag{12}$$

The normal distance of the 15^{th} node is represented by y_n (see Eq. 15). The following equation is used to calculate the corresponding value of the boundary layer thickness for a given value of Re and L.

$$\delta = 0.035\, LRe_L^{-\frac{1}{7}} \tag{13}$$

The boundary layer thickness obtained from Eq. (13) is then assigned to $y_n(n_{min})$ and the mesh growth rate (r_m) is determined from the wall side using the geometric progression formula given in Eq. (15) to ensure that it is within n_{min}, which lies within the boundary layer thickness.

$$\boldsymbol{r_m = \left[\frac{y_N(n_{min})}{\Delta y}\right]^{1/(n_{min}-1)}} \tag{14}$$

$$r_m = \left[\frac{y_n(15)}{\Delta y}\right]^{1/14} \tag{15}$$

Boundary Conditions and Validation

The T-56 Engine compressor rotor was simulated using a computational domain consisting of a single rotor passage. To save computational resources and time, periodic conditions were

used to simulate the behavior of the entire compressor. A strong set of boundary conditions, including total pressure inlet and static pressure outlet conditions, were applied to the inlet and outlet of the computational domain. As shown in Fig 4, The bounding surfaces of the passage were subjected to rotational periodicity in the θ direction. The shroud wall was modeled as a stationary wall, while the rotor and hub walls were modeled as rotating domains. In addition, the rotor, hub, and shroud walls were modeled with no-slip wall conditions. To analyze the impact of erosion rate on the performance of the transonic compressor rotor, measurements were taken for P_r, P_c and d_P. The rotor's rotational speed was kept constant at its design value of 13,829.96 rpm.

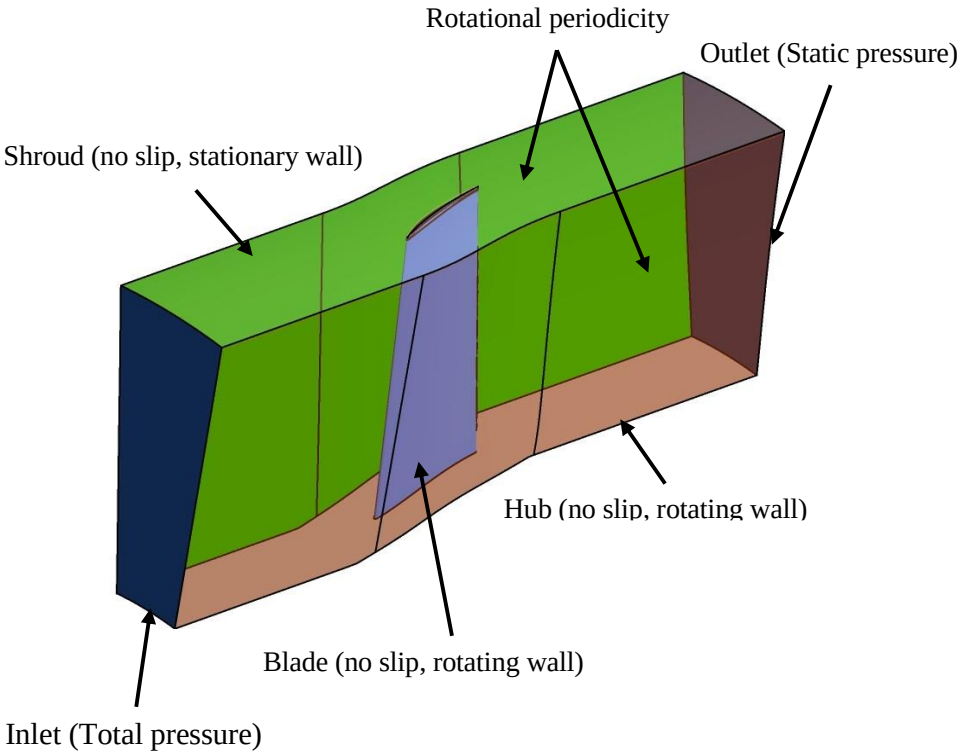

Fig 2: Details of the Imposed Boundary Conditions

VALIDATION OF THE COMPUTATIONAL MODEL

Due to the lack of experimental data, the computational model used in this study was validated using the previously examined geometry of NASA's rotor 37 [12]. At a mass flow rate of 20.19 kg/s, the rotor's design pressure ratio is 2.106, while the measured limiting mass flow is 20.93 kg/s. At the design wheel speed of 17,188.65 rpm, the relative Mach number at the hub is 1.13 and at the tip inlets is 1.48, resulting in a nominal tip speed of 454 m/s. The rotor has 36 blades with an aspect ratio of 1.19, hub-to-tip ratio of 0.70, and tip solidity of 1.288. The running tip clearance was assessed to be 0.356 mm (0.5% span).

The numerical and experimental findings are compared in Table 1, and the pressure ratio profile is compared in Fig. 5. The results show that the computational model established in this

study can be used to further examine erosion effects, with close agreement between the numerical and experimental data.

Table 1: Comparison of the Numerical and Experimental Results

Pressure ratio			Efficiency			Mass flow rate		
Experimental	Numerical	% Age difference	Experimental	Numerical	% Age difference	Experimental	Numerical	% Age difference
2.11	1.98	-5.98	0.92	0.89	3.26	20.19	19.97	1.09

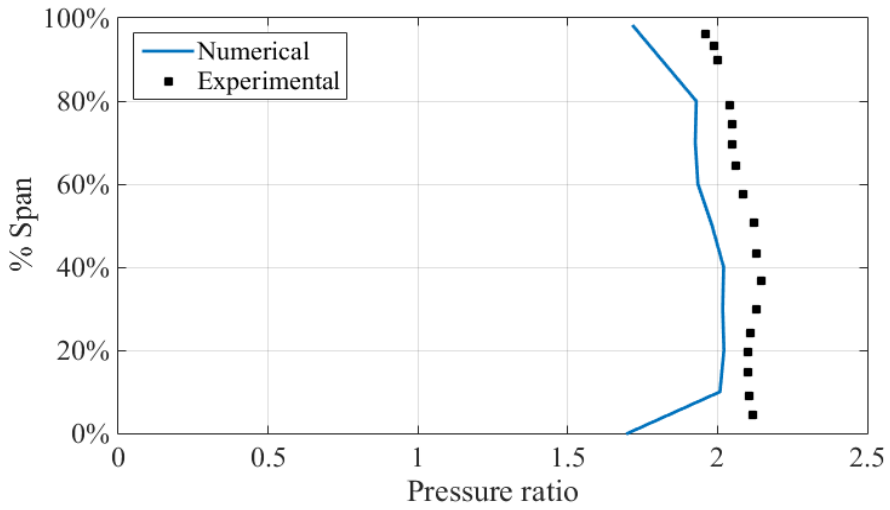

Fig 3: Pressure Ratio Comparison between the Experimental and Numerical Results at the Exit Plane

RESULTS AND DISCUSSIONS

Quantitative displays of the Mach number and erosion rate density contours are shown in Figs. 6 and 7, respectively. Fig 6 depicts contours on a turbo surface extracted at different span locations (5%, 25%, 50%, and 75%). It can be observed that the Mach number is greater than one for all span locations, leading to the formation of a bow shock wave from the leading edge of the blade. A recirculation and separation zone is formed due to the wake of the bow shock wave, which can be observed in the contours for all span locations. Due to the larger shock wave generated by the higher Mach number at higher span locations, the separation zone grows. Since the tangential velocity component grows as a function of blade height ($V_t = r\,\omega$), the Mach number grows as the blades' spans do. The low-pressure and high-pressure sides of the blades' erosion rate density contours are shown in Fig. 7. On the high-pressure side of the blade, the erosion rate density is much higher than on the low-pressure side. The concentration of red spots in the hub and shroud regions indicates that these areas are most susceptible to erosion rates. However, simulation results suggest that the tip region is the most affected area by erosion, encompassing 90% to 100% of the blade span location.

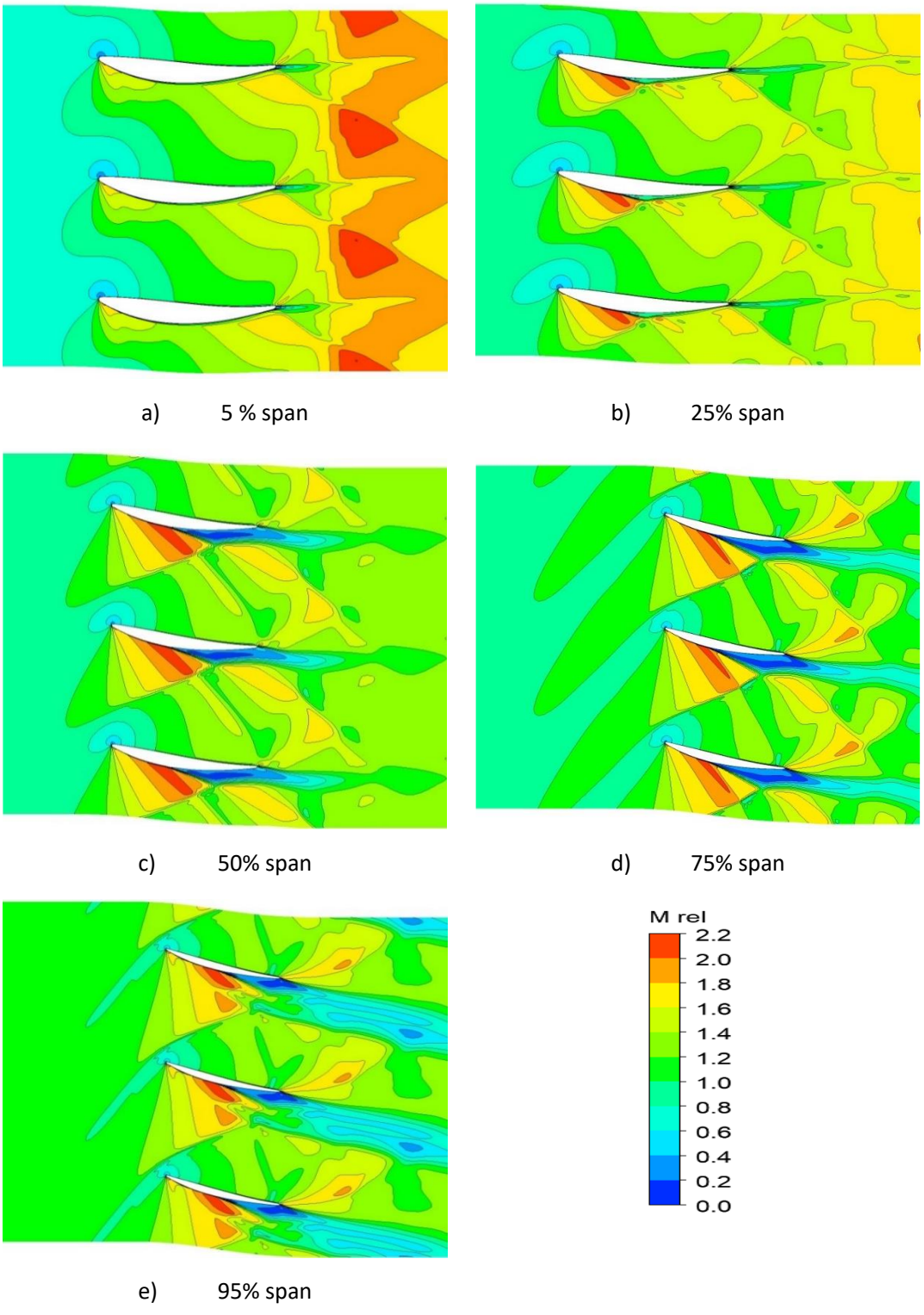

Fig 4: Contours of the Relative Values of the Mach Number Extracted from Different Span Locations

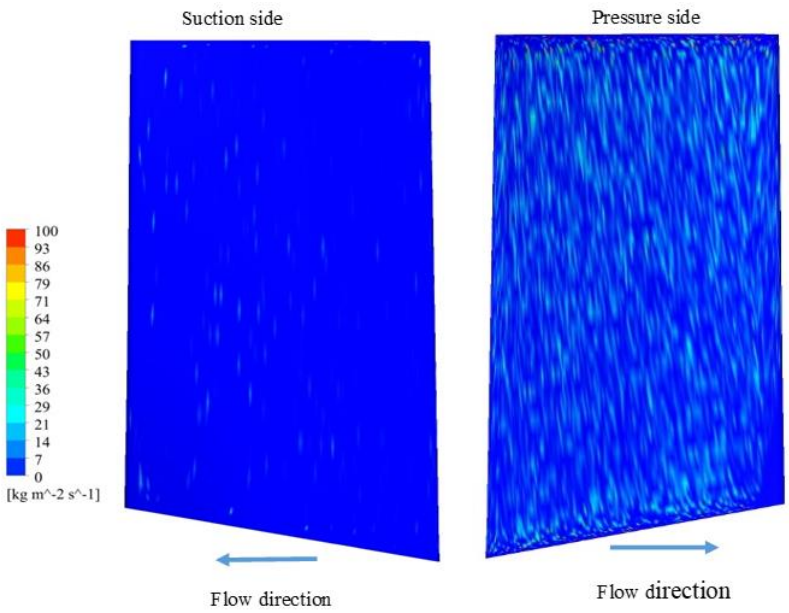

Fig 5: Erosion Rate Density Contours Plots on the Suction and Pressure Sides

Effect of Compressor Pressure Ratio on the Erosion Characteristics of the Blade

This section discusses how the concentration of sand particles affects the erosion behavior of compressor blades. Six different sand particle concentrations, ranging from 2.5% to 25%, were tested. Fig. 8 depicts the pressure blade loading with and without sand particles. Fig. 8 (a) illustrates the pressure loading without sand particles, while Fig. 8 (b) shows the pressure loading with 20% sand particle concentration in the working fluid (air). When the quantity of sand particles in the air is increased, the pressure loading on the blade decreases significantly, as seen by the comparison of the two figures. Additionally, the deterioration in performance is observed to increase with the rise in pressure ratio across the compressor.

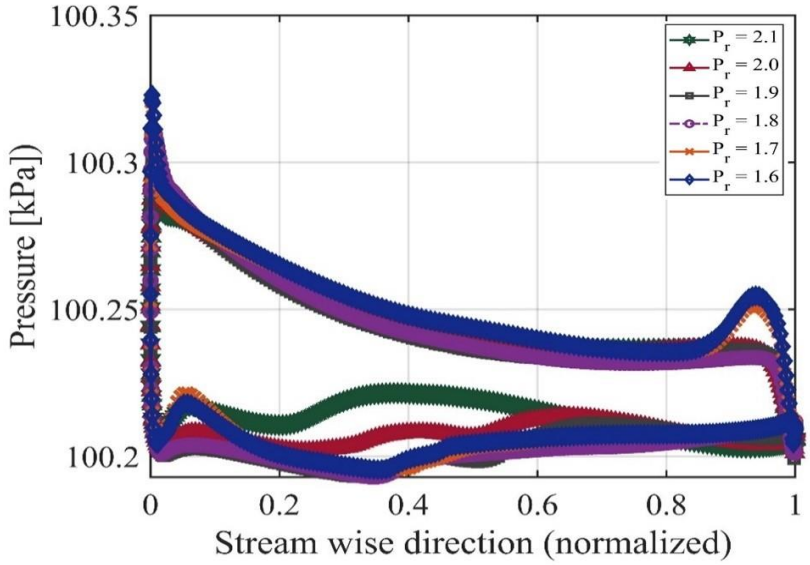

Fig 6 (a) Pressure Loading of the Blade at 50% Span without Solid Particles

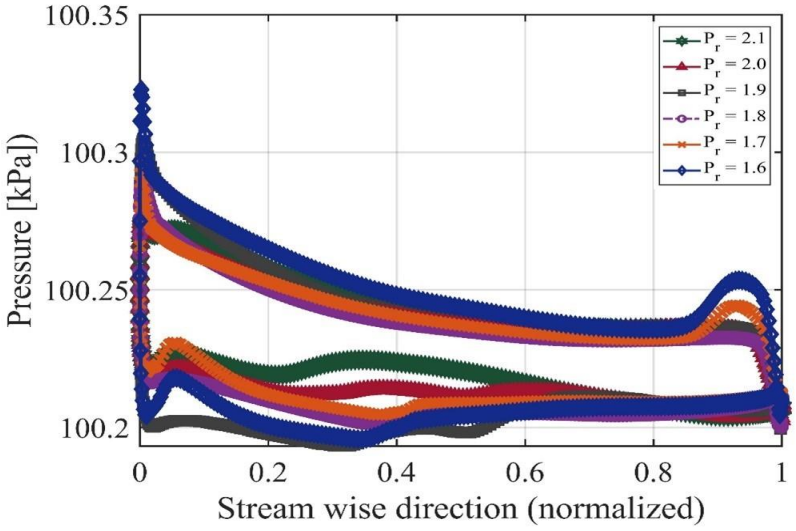

Fig 8 (b) Pressure Loading of the Blade at 50% Span Using 20% Concentration of the Solid Particles

The variation of particle momentum source along the streamwise direction from air to solid particles is depicted in Fig 9(a). The profiles in Fig 9 (b) are calculated by averaging the variations on each polyline at various span locations. The single line in Fig 9 (a) represents the average behavior of erosion characteristics along the span-wise orientation of the blade. The profile has two peaks, one immediately downstream of the leading edge and the other just upstream of it, and it varies slightly with the pressure ratio. Similarly, Fig. 10 depicts the wall stress values resulting from particle collisions with blade walls, which exhibit a similar trajectory to the particle momentum transfer. Variation of the particle momentum transfer value with respect to the pressure ratio and blade length is negligible. In addition, Fig. 11 illustrates the profiles of erosion rate densities in the streamwise direction on the blade for various pressure ratios. The erosion rate density values vary considerably along the streamwise direction, exhibiting two maxima downstream of the leading edge and near the trailing edge of the blade. The maximum erosion rate density value is computed against the minimum pressure decrease across the rotor, i.e., 1.6, then 1.7. However, for pressure ratios greater than 1.7, the profiles and magnitudes of erosion rate density are nearly identical, indicating that erosion rate density values are sensitive to decreasing pressure ratio values across the compressor. The erosion rate density does not vary significantly with the pressure ratio value at greater pressure ratios.

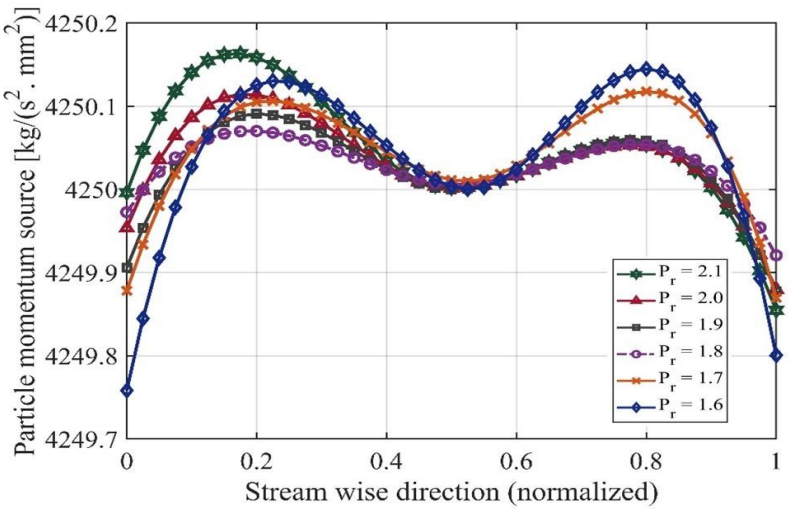

Fig 7 (a) Variation in the Particle's Momentum Source Along the Streamwise Direction on the Blade

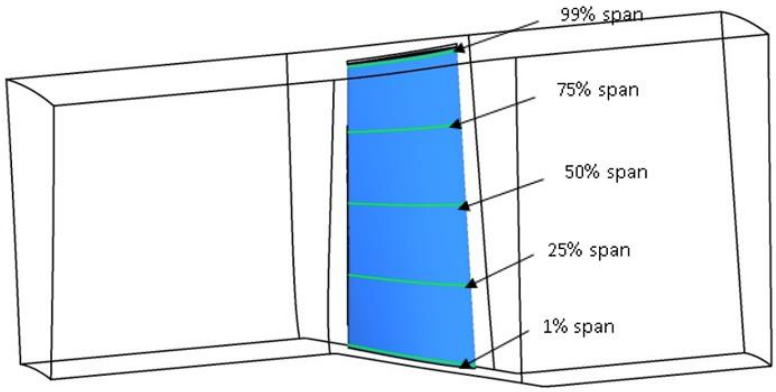

Fig 9 (b) Polyline Locations at Various Span Locations, i.e., 1%, 5%, 25%, 50%, 75% and 99% Respectively

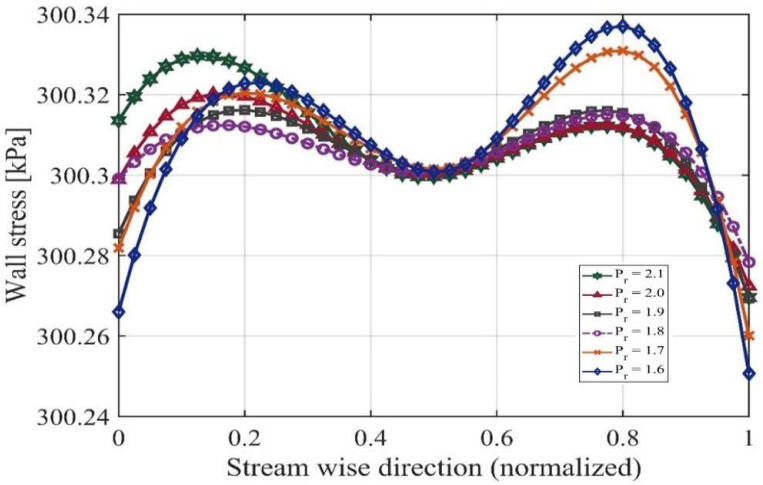

Fig 8 Profiles of Wall Stress in the Streamwise Direction on the Blade Corresponding to Different Values of the Pressure Ratio

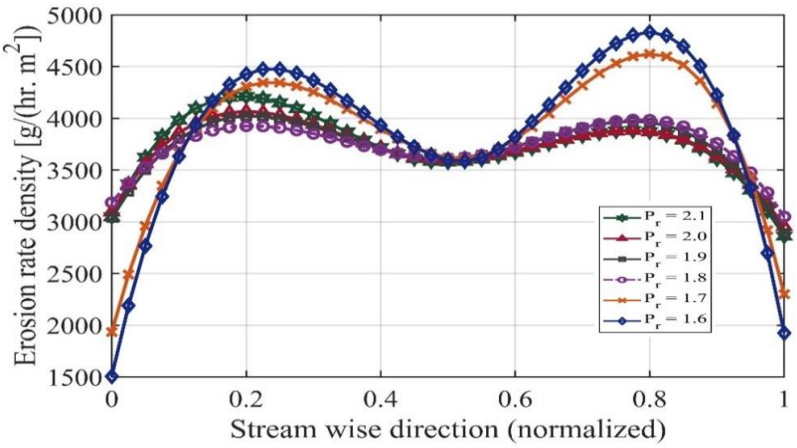

Fig 9 Profiles of Erosion Rate Densities in the Streamwise Direction on the Blade Corresponding to Different Values of the Pressure Ratio

The graph in Fig. 12 depicts the density of the average erosion rate on the surface of the blades versus the pressure ratio. The highest erosion rate density (3,894 g/hr.m2) was observed for the lowest pressure ratio studied (1.6). As the ratio of pressure increased from 1.6 to 1.8, the density of the erosion rate decreased rapidly. However, for further increases in the pressure ratio, there was no significant change in the erosion rate density. This indicates that the erosion rate density is extremely sensitive to low pressure ratios, but the effect diminishes with increasing pressure ratios.

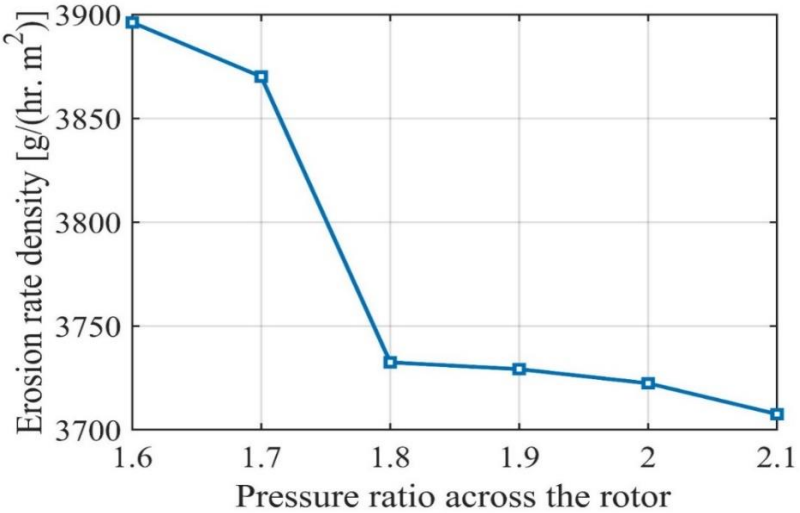

Fig 10 Variation in the Value of the Blade Averaged Erosion Rate Density with the Pressure Ratio Across the Compressor

Effect of Particle's Concentration on the Erosion Characteristics of the Blade

Figures 13 through 16 provide a comprehensive analysis of the effect of airborne particle concentrations on the rotor blade erosion characteristics. Fig 13 illustrates the tendencies of particle momentum source on the blade's surface in the streamwise direction for various

particle concentrations, including 2.5%, 5%, 10%, 15%, 20%, and 25%. The graph clearly demonstrates that the source of particle momentum is significantly affected by particle concentration and streamwise direction. At a particle concentration of 15 percent, the source of particle momentum reaches its optimum. As the particle concentration continues to increase, the source of particle momentum begins to decrease. Notably, the maximum local values of the particle momentum source are observed just downstream of the leading edge for a 25% concentration. It is worth mentioning that the variation along the streamwise direction is most pronounced at the highest particle concentration (25%) while it is comparatively minimal at lower concentrations.

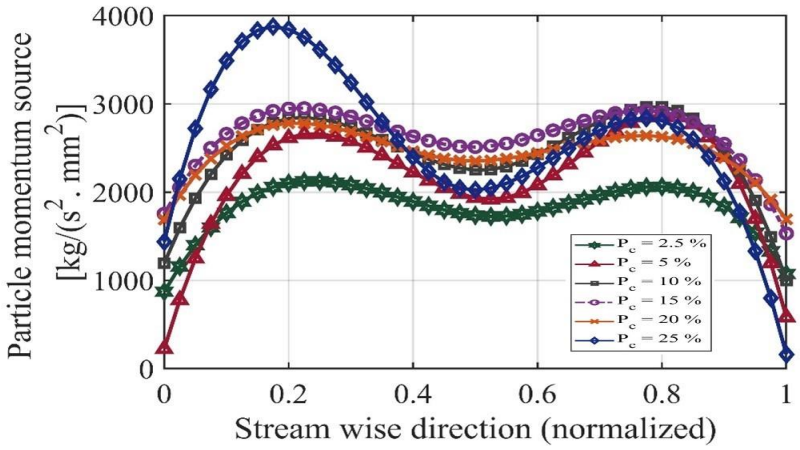

Fig 11 Profiles Particles Momentum in the Streamwise Direction on the Blade Corresponding to Different Values of the Concentration of the Particles

Fig 14 depicts the profiles of wall stress in the streamwise direction on the blade for various particle concentrations. The trends observed in the momentum transfer term are consistent with the wall stress values caused by the particles. Once the maximum values at 15% particle concentration are attained, the wall stress values rise in tandem with the particle momentum source values. As the concentration of particles continues to increase, the wall stress values begin to decrease. However, the variation of the wall stress values along the streamwise direction remains essentially the same. Notably, the rate of increase in wall stress values is considerably greater as the particle concentration rises from 2.5% to 15%, while the rate of decrease in wall stress values is relatively slower as the particle concentration rises from 15% to 25%.

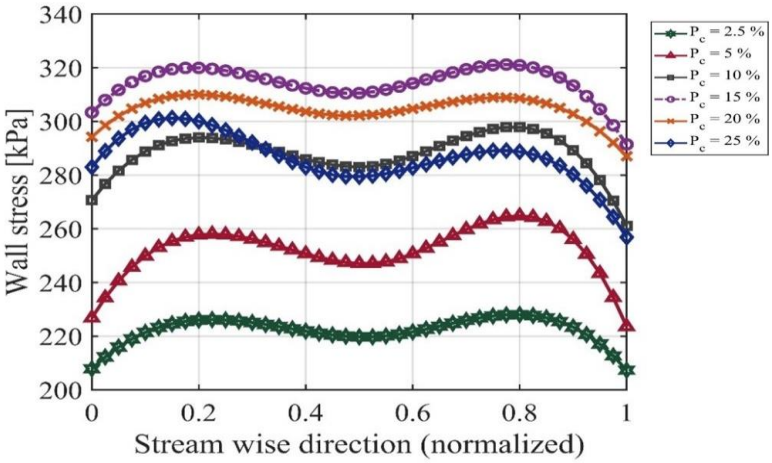

Fig 12: Profiles of the Wall Stress in the Streamwise Direction on the Blade Corresponding to Different Values of the Concentration of the particles

The profiles of erosion rate densities in the streamwise direction on the blade for various particle concentration values are depicted in Fig. 15. The observed trends in erosion rate density correspond to those previously discussed for the momentum transfer term and wall stress term. The erosion rate density initially increases with increasing particle momentum source values until it reaches its maximal value at a particle concentration of 15%. As the particle concentration continues to rise, the density of the erosion rate begins to decrease. In Fig. 16, the average blade value of the erosion rate density increases as the particulate concentration rises. In particular, the average erosion rate density of the blade increases from 29,000 to 41,000 g/hr.m2 as the particulate concentration rises from 2.5% to 15%. The erosion rate density decreases to 41,000 g/h/m2 when the particle concentration is increased from 15% to 25%.

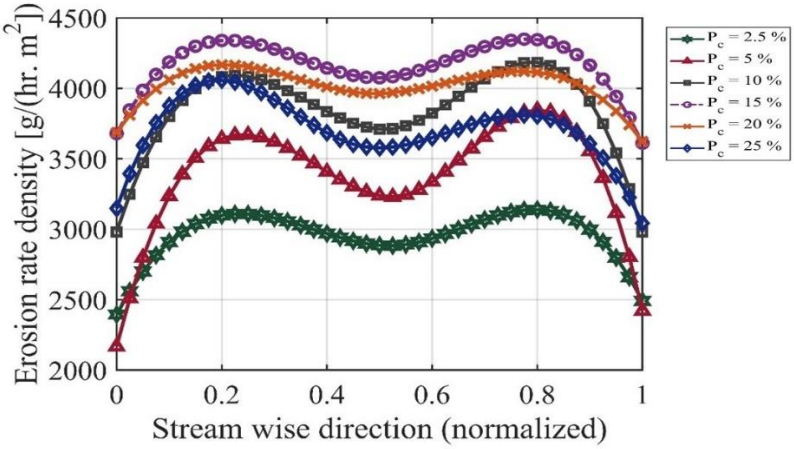

Fig 13: Profiles of Erosion Rate Densities in the Streamwise Direction on the Blade Corresponding to Different Values of the Concentration of the Particles

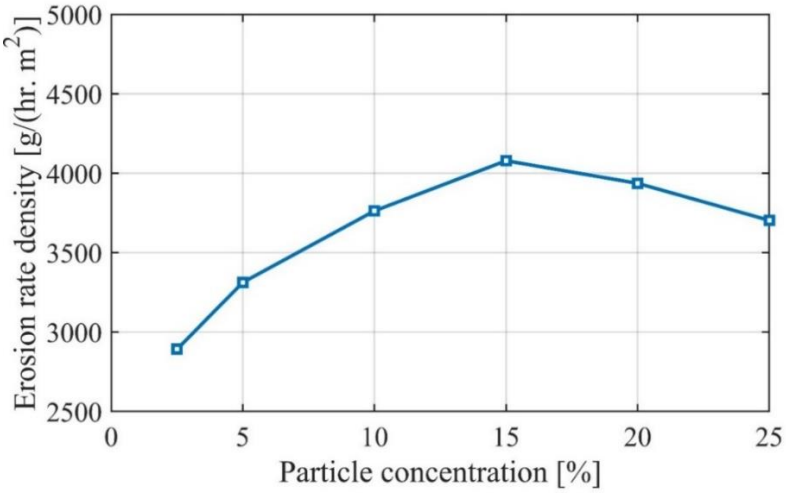

Fig 14: Variation in the Value of the Blade Averaged Erosion Rate Density with Different Values of the Concentration of the Particles

Figures 17 and 18 depict the profiles of wall stress and erosion rate density in the streamwise direction on the blade for various sand particle sizes. By examining the data in these figures along with the specified particle sizes and referring to Table 2 for the investigated conditions, it is evident that both wall stress and erosion rate density increase as particle size increases. Additionally, along the streamwise direction, considerable variations in wall stress and erosion rate density can be observed, mirroring the trends observed for particle concentration and pressure ratio. Moreover, based on the data presented in Fig. 19, it can be observed that the blade-averaged value of the erosion rate density increases significantly as particle size increases. Initially, as the particle size increases from Size A to Size D, the density of the erosion rate increases significantly. However, as particle size increases, the rate of increase in erosion rate density becomes relatively less rapid.

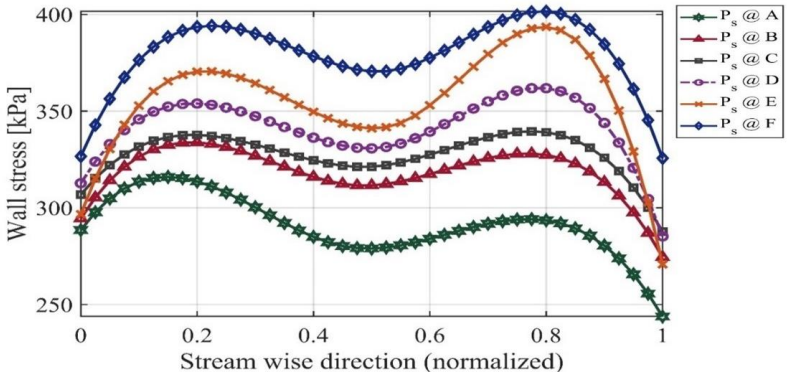

Fig 15: Profiles of Wall Stress in the Streamwise Direction on the Blade Corresponding to Different Sizes of the Sand Particles

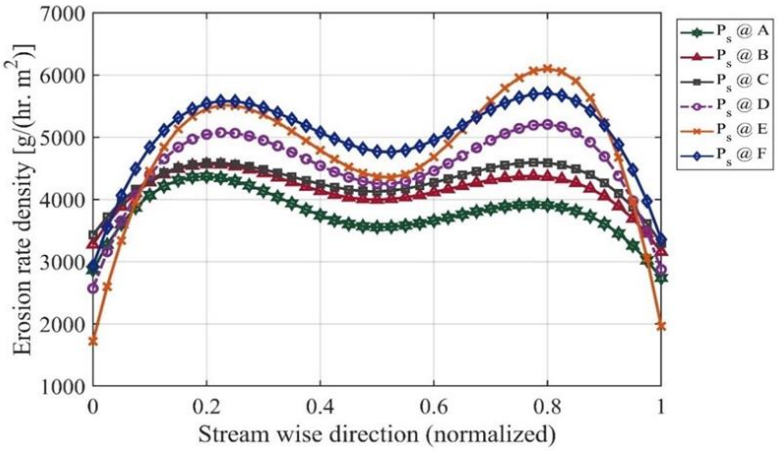

Fig 16: Profiles of Erosion Rate Densities in the Streamwise Direction on the Blade Corresponding to Different Sizes of the Sand Particles

Table 2: List of the Conditions Studied

Simulations	Pressure ratio P_r	Particle concentration	Particle distribution [micron]				
				Min	Max	Ave	Std. dev.
1	1.6	2.5%	A	50	250	150	120
2	1.7	5%	B	100	500	150	120
3	1.8	10%	C	150	750	150	120
4	1.9	15%	D	200	1000	150	120
5	2.0	20%	E	250	1250	150	120
6	2.1	25%	F	250	1250	150	120

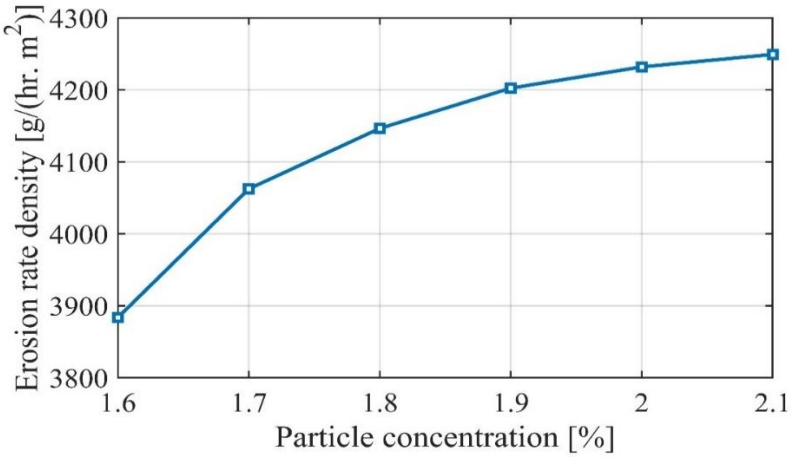

Fig 17 Variation in the Value of the Blade Averaged Erosion Rate Density with Different Sizes of the Sand Particles

CONCLUSIONS

In this study, a numerical simulation was used to analyze the first stage of a C-130 T-56 engine compressor rotor and to investigate the effects of pressure ratio, mass concentration, and particle size on erosion rate and performance. Due to the lack of experimental data for the

geometry, a 3D scan was conducted to collect profile data from both the new and eroded blades of the T-56 first stage compressor. The computational model employed in this analysis was validated using the NASA Rotor 37 model approach. This approach had previously been employed in our previous study [12].

The simulation results indicated that the Mach number exceeded one at all span locations, resulting in the formation of a bow shock wave at the blade's leading edge. In addition, it was observed that the separation region expanded as spanwise locations increased. This expansion can be attributed to the stronger shock wave at greater spans, which is the result of higher Mach numbers resulting from increased tangential velocity components with blade height. Compared to the high-pressure side, the low-pressure side of the blade experienced lesser erosion rates, with the hub and shroud regions being especially susceptible to erosion. However, the blade's tip region, spanning from 90 to 100%, was identified as the most vulnerable to erosion.

In addition, it was found that as the concentration of sand particles in the air increases, the pressure loading of the blade deteriorates significantly. Moreover, this performance degradation becomes more pronounced as the pressure ratio across the compressor increases. The analysis of the particle momentum source revealed significant variations in particle concentration and streamwise direction behavior. As particle concentration increases, so does the source of their momentum. The tendencies observed in the variation of particle-caused wall stress values align with those of the momentum transfer term. With an increase in momentum source values and particle concentrations, the wall stress values increase. However, wall stress variation along the streamwise direction remains constant.

Patterns comparable to the momentum transfer term and wall stress term were observed for the erosion rate density with respect to particle concentration. The erosion rate density initially increased with increasing momentum source values, reached a limit, and then decreased as the particle concentration increased further. Furthermore, both wall stress and erosion rate density increased as particle size increased. Notably, variations in terms of wall stress and erosion rate density were also observed along the streamwise direction, reflecting the trends observed in particulate concentration and pressure ratio.

Finally, it is essential to note that the blade-averaged erosion rate density experiences a rapid increase with larger particle sizes, although the rate of increase becomes relatively smaller with further particle size increments. The trends of wall stress and eroding rate density are consistent with respect to the pressure ratio, particle concentration, and particle size.

RECOMMENDATIONS

The utilization of the same computational fluid dynamics (CFD) model will enable the analysis of particle behavior and the assessment of multiple compressor stages or rotor-stator interactions. The presented comprehensive approach allows for the investigation of various factors such as heat transfer, blade wall deformation, and the impact of metal blade fatigue modes, including low cycle fatigue (LCF), high cycle fatigue (HCF), and very high cycle fatigue (VHCF). By considering these aspects, a holistic understanding of the compressor's performance and durability can be achieved. It is essential to recognize that the degradation of

compressor performance can have significant implications for engine efficiency and overall performance. Changes in blade surfaces, tip leaks, and variations in blade pressure distribution can adversely affect the engine's operation. To accurately simulate real-world conditions, these factors can be incorporated into the numerical model, providing a comprehensive analysis of compressor performance.

Furthermore, the developed numerical model can be employed to investigate the effects of foreign object damage or bird strikes on compressor blades. By studying these scenarios, potential strategies for mitigating damage and enhancing blade integrity can be explored. Future investigations could focus on evaluating the resistance of compressor blade coatings to sand particles. This research area holds promise for enhancing the durability and lifespan of compressor blades in environments prone to contamination.

ACKNOWLEDGMENT

This project was funded by the Deanship of Scientific Research (DSR), King Abdulaziz University, Jeddah, under grant No. (DF-171-135-1441). The authors, therefore, gratefully acknowledge DSR technical and financial support.

Nomenclature

C_f	fluid volume concentrations
C_s	solid volume concentrations
d_P	particle size
E	dimensionless mass
$F_{l,f}$	lift force for fluid phases
F_l, s	lift force for solid phases
$F_{vm,s}$	virtual mass force per unit mass for fluid and solid phases
$f(\gamma)$	angle of impact in radians
L	flow length scale reynolds number
m_a	flow rate of air
m_P	particle mass concentration
n_{min}	minimum number of nodes
p	mean value of pressure assigned for the interface between solid and fluid phase
Pc	particle mass concentration
Pr	pressure ratio
ρ_f	densities of the fluid phase
ρ_s	densities of the solid phase
R	interaction force between the two phases
r	radius
r_m	mesh growth rate
rpm	rotations per minute
SST	shear stress transport model
V_f	velocity vector
V_p	particle velocity

V_t	tangential velocity
ω	angular velocity
y_n	normal distance
Δy	distance of the first node from the wall
τ_f	shear stress
δ	boundary layer thickness

References

[1] Rolls-Royce corporation, 'T-56/50D Desert operation presentation Engine safety brief.', Dallas.

[2] M. Suzuki, K. Inaba, and M. Yamamoto, 'Numerical simulation of sand erosion phenomena in rotor/stator interaction of compressor', Journal of Thermal Science, vol. 17, pp. 125–133, 2008.

[3] M. Suzuki and M. Yamamoto, 'Numerical simulation of sand erosion phenomena in a single-stage axial compressor', Journal of Fluid Science and Technology, vol. 6, no. 1, pp. 98–113, 2011.

[4] S. Elfeki and W. Tabakoff, 'Erosion Study of Radial Flow Compressor with Splitters', in Turbo Expo: Power for Land, Sea, and Air, American Society of Mechanical Engineers, 1986, p. V003T05A002.

[5] J.-P. Immarigeon, D. Chow, V. R. Parameswaran, P. Au, H. Saari, and A. K. Koul, 'Erosion testing of coatings for aero engine compressor components', Advanced Performance Materials, vol. 4, pp. 371–388, 1997.

[6] E. N. Kablov and S. A. Muboyadzhyan, 'Erosion-resistant coatings for gas turbine engine compressor blades', Russian Metallurgy (Metally), vol. 2017, no. 6, pp. 494–504, Jun. 2017, DOI: 10.1134/S0036029517060118.

[7] M. W. Reedy, T. J. Eden, J. K. Potter, and D. E. Wolfe, 'Erosion performance and characterization of nanolayer (Ti,Cr)N hard coatings for gas turbine engine compressor blade applications', Surf Coat Technol, vol. 206, no. 2–3, pp. 464–472, Oct. 2011, DOI: 10.1016/j.surfcoat.2011.07.063.

[8] J. S. Litt and D. L. Simon, 'Toward a real-time measurement-based system for estimation of helicopter engine degradation due to compressor erosion', Journal of the American Helicopter Society, vol. 54, no. 1, p. 12008, 2009.

[9] A. Hamed, W. Tabakoff, and D. Singh, 'Modeling of compressor performance deterioration due to erosion', International Journal of Rotating Machinery, vol. 4, no. 4, pp. 243–248, 1998, DOI: 10.1155/S1023621X98000207.

[10] W. Tabakoff, A. N. Lakshminarasimha, and M. Pasin, 'Simulation of compressor performance deterioration due to erosion', J Turbomach, vol. 112, no. 1, pp. 78–83, 1990, Doi: 10.1115/1.2927424.

[11] W. Tabakoff, 'Performance Deterioration', 2014.

[12] N. A. Qattan, A. M. Al-Bahi, and B. Kada, 'Simulation of Transonic Compressor Performance Deterioration Due to Sand Erosion'. [Online]. Available: http://asrjetsjournal.org/

[13] H. K. Versteeg and W. Malalasekera, An introduction to computational fluid dynamics: the finite volume method. Pearson education, 2007.

[14] K. V Pagalthivarthi, P. K. Gupta, V. Tyagi, and M. R. Ravi, 'CFD predictions of dense slurry flow in centrifugal pump casings', International journal of aerospace and mechanical engineering, vol. 5, no. 4, pp. 16–28, 2011.

[15] G. Brown, 'Use of CFD to predict and reduce erosion in an industrial slurry piping system', in Fifth International Conference on CFD in the process industries. CSIRO, Melbourne, Australia, 2006, pp. 13–15.

[16] G. J. W. Van Bussel, 'The science of making more torque from wind: Diffuser experiments and theory revisited.', in Journal of Physics: Conference Series, IOP Publishing, 2007, p. 012010.

[17] M. Saeed and M.-H. Kim, 'Airborne wind turbine shell behavior prediction under various wind conditions using strongly coupled fluid structure interaction formulation', Energy Convers Manag, vol. 120, pp. 217–228, 2016.

[18] M. O. L. Hansen, N. N. Sørensen, and R. G. J. Flay, 'Effect of placing a diffuser around a wind turbine', Wind Energy: An International Journal for Progress and Applications in Wind Power Conversion Technology, vol. 3, no. 4, pp. 207–213, 2000.

[19] F. R. Menter, 'S. Eloret Institute, Zonal two equation kappa-omega turbulence models for aerodynamic flows', in 24th Fluid Dynamics Conference, 1993.

[20] I. M. Hutchings, 'Mechanical and metallurgical aspects of the erosion of metals', in Corrosion/Erosion of Coal Conversion Systems Materials Conference, 1979, pp. 393–428.

[21] I. Finnie, 'Some observations on the erosion of ductile metals', wear, vol. 19, no. 1, pp. 81–90, 1972.

[22] C. F. X. Ansys, 'CFX-Pre user's guide release 16.0', Ansys Inc.: Canonsburg, PA, USA, 2015.

[23] S. Z. Roshan, S. Alimirzazadeh, and M. Rad, 'RANS simulations of the stepped duct effect on the performance of ducted wind turbine', Journal of Wind Engineering and Industrial Aerodynamics, vol. 145, pp. 270–279, 2015.